Parametric Evaluation of Thin, Transonic Circulation-Control Airfoils

Robin Schlecht* and Scott Anders*
NASA Langley Research Center, Hampton, Virginia, 23681-2199

Wind-tunnel tests were conducted in the NASA Langley Transonic Dynamics Tunnel on a 6 percent-thick, elliptical circulation-control airfoil with upper-surface and lower-surface blowing capability. Results for elliptical Coanda trailing-edge geometries, biconvex Coanda trailing-edge geometries, and leading-edge geometries are reported. Results are presented at subsonic and transonic Mach numbers of 0.3 and 0.8, respectively. When considering one fixed trailing-edge geometry, for both the subsonic and transonic conditions it was found that the [3.0:1] ratio elliptical Coanda surface with the most rounded leading-edge [03] performed favorably and was determined to be the best compromise between comparable configurations that took advantage of the Coanda effect. This configuration generated a maximum $C_l = 0.625$ at a $C_\mu = 0.06$ at M = 0.3, = 6 . This same configuration generated a maximum $C_l = 0.275$ at a $C_\mu = 0.0085$ at M = 0.8, = 3 .

Nomenclature

	= Angle-of-attack
b	= Span
c	= Chord length
C_d	= Sectional drag coefficient
$C_{d_{rake}}$	= Uncorrected drag measured at the wake rake
C_l	= Sectional lift coefficient
C_m	= Sectional pitching moment coefficient, 25 percent chord
c_{ref}	= Reference chord, 30 inches
C_μ	= Momentum coefficient
C_p	= Pressure coefficient
C_{p_l}	= Lower C_p
C_{p_u}	= Upper C_p
C_p^*	= Pressure coefficient at locally sonic conditions
ΔC_l	= Sectional lift increment
ΔC_d	= Sectional drag increment
Δh	= Incremental height distance
γ	= Ratio of specific heat
LE	= Leading-edge
M	= Mach number
$\dot{m}$	= Mass flow rate
p	= Static pressure
p_o	= Total pressure
$p_{o_{jet}}$	= Total pressure of the jet
p_{o_∞}	= Total pressure of the freestream
p_∞	= Freestream static pressure
R	= Gas constant for air
Re	= Reynolds number
S	= Planform area

*Aerospace Engineer, Advanced Aerospace Systems Branch, 16 Victory Street/Mail Stop 411.

TDT = Transonic Dynamics Tunnel
TE = Trailing-edge
$T_{o_{jet}}$ = Total temperature of the jet
U_{jet} = Jet velocity
V_∞ = Freestream velocity
x = Chordwise distance measured from reference airfoil leading-edge
y = Spanwise distance measured from the wing root
z = Vertical distance measured from reference airfoil chord-line

I. Introduction

It has been shown that circulation-control is an effective method for providing large lift augmentation.[1,2] Lift coefficients as high as nine have been achieved in 2D wind-tunnel experiments.[3] The concept of circulation-control dates back to the 1930's when Henry Coanda claimed to discover it.[4,5,6] The technique, as used here, augments an airfoil's lifting capability by tangentially ejecting a thin jet of high momentum air over a rounded trailing-edge.[7] When the jet sheet velocity is greater than the local external flow, separation is delayed by means of the Coanda effect.[8,9,10] The Coanda effect is created when a jet of air is blown tangentially over a curved or "Coanda" surface and remains attached to the surface due to a balance between the low static pressures generated by the jet and the centrifugal force acting on the curving jet.[11] The Coanda effect results in the movement of the separation point around the trailing-edge toward the lower-surface of the wing and also entrains the external flow field. This produces a net increase in the circulation of the wing resulting in lift augmentation.[12] Historically circulation control has been primarily used for lift augmentation by blowing out of a single slot on the upper-surface. However, the focus of this investigation is to see how effectively circulation control can be used to generate control power at transonic conditions by making use of the Coanda effect at low momentum coefficients. This can be achieved by using an upper and lower slot and applying differential blowing or by blowing over the upper or lower Coanda surface independently. This body of work evaluates the effectiveness of circulation-control on a thin airfoil section at a Mach number (M) of 0.8. Results at Mach number of 0.3 are also included and are considered important for evaluation of the trade-off between low-speed versus high-speed effectiveness.

Numerous experimental circulation-control tests using the Coanda effect to enhance lift have been conducted at subsonic velocities on thick airfoil sections.[13,14,15,16,17,18,19] The technology has also been flight tested at low-speed conditions on an A-6 in 1979.[20,21,22] In addition, a limited amount of circulation-control research has been conducted at low transonic conditions. However, the research was constrained to airfoils that were on the order of 15 to 18 percent-thick. The focus was on helicopter rotor blade applications and was typically limited to maximum Mach numbers between 0.6 and 0.7. Despite the large body of circulation-control research found in the literature, a void exists for higher Mach number data on thin airfoils.

Three wind-tunnel tests have been conducted on a 6 percent-thick, 0.75 percent cambered, elliptical airfoil with both upper-surface and lower-surface slot blowing capability. Parametric evaluations of jet slot heights and Coanda surface shapes were conducted during the first wind-tunnel test. The results of the first test were reported by Alexander.[23] The second and third wind-tunnel tests continued with additional evaluations of elliptical Coanda trailing-edge geometries, biconvex Coanda trailing-edge geometries, leading-edge geometries, and jet-flap configurations. The optimum slot height found from the first test entry was used for all configurations tested during the second and third wind-tunnel tests. Evaluations were made at momentum coefficients (C_μ) up to 0.12. Test data were acquired at Mach numbers of 0.3, 0.5, 0.7, 0.8, and 0.84 at Reynolds numbers (Re) per foot of 2.43×10^5 to 1.05×10^6. The data reported in this paper includes an evaluation of performance for upper-surface and lower-surface blowing for elliptical Coanda trailing-edge geometries, biconvex Coanda trailing-edge geometries, and leading-edge geometries. Results are presented at subsonic and transonic Mach numbers of 0.3 and 0.8, respectively.

II. Model and Facility Description

The model tested in this experimental investigation was an unswept, semi-span circulation-control airfoil with a rectangular planform. A photograph of the circulation-control airfoil mounted in the NASA Langley Research Center's Transonic Dynamics Tunnel (TDT) is shown in Fig. 1. The reference airfoil section that all configurations were based on was a 30 inch chord, 6 percent-thick, elliptical airfoil with 0.75 percent camber. The last three inches of the reference airfoil were removed and replaced with Coanda trailing-edge geometries. The leading-edge could also be replaced with alternate designs. The model was mounted in the TDT on a sidewall turntable that protruded through a large splitter plate located approximately forty inches from the tunnel wall. A circular end plate was mounted on the wing tip to help promote two-dimensional flow. Boundary-layer trip strips were installed 1.5 inches

from the leading-edge on the upper and lower-surfaces. The trip strips consisted of 0.038 inch diameter epoxy dots with a thickness of 0.015 inch and an edge-to-edge spacing of 0.098 inches. Circulation-control was achieved on the model by blowing tangentially from either the upper or lower full-span rectangular slot located at the beginning of the trailing-edge, or "Coanda surface." The optimum slot height was previously found to be 0.03 inches (y/c_{ref} = 0.001), and is shown in Fig. 2 and Fig. 3. The slots were located at x/c_{ref} = 0.9 and extended the full-span (60 inches) of the model. The upper and lower slot plenums contained a thirty percent porosity screen located 5.4 inches upstream of the slot exit that helped provide better flow uniformity across the slot span. The two plenums were fed by separate supply lines that had remotely controlled motorized valves. The supply system was capable of providing up to 1 lbm/sec of air. For further details of this model, please refer to the NASA TM that documents the first test entry.[23]

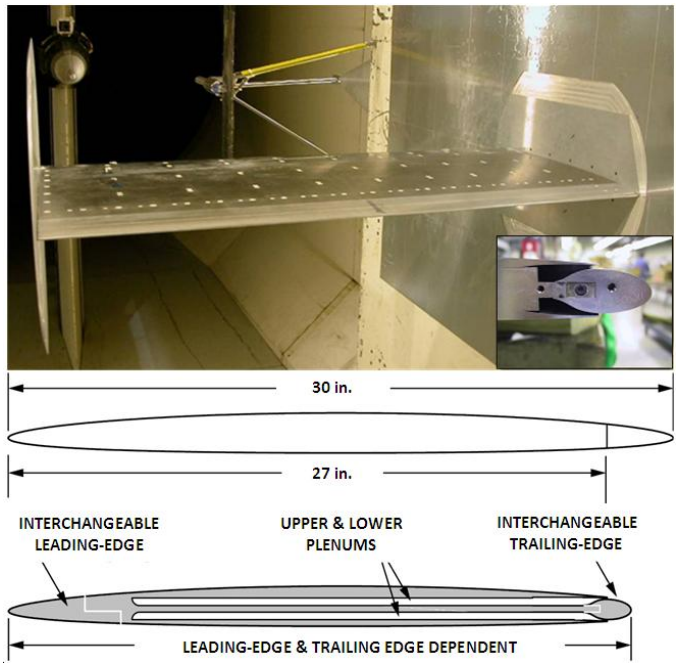

Figure 1. Quasi-2D, un-swept, rectangular CCA wing.

III. Instrumentation and Calculation of Coefficients

The circulation-control airfoil was instrumented with a total of 157 static and total pressure taps, one accelerometer near the wing tip, and one thermocouple in each plenum. There were also two spanwise rows of ten static pressures taps each that were located at x/c_{ref} = 0.5 and at 0.8 on the upper and lower airfoil surface. The sectional lift and pitching moment coefficients were calculated from the pressure measurements. This model did not have a balance installed in it. An 87-probe wake rake was located one reference chord length downstream of the CCA trailing-edge and was used to calculate drag. The momentum coefficient (C_μ) was calculated using plenum pressure measurements and the mass flow found from Venturi flow meters that were installed in each supply line.

A. Sectional Lift and Pitching Moment Coefficient, C_l and C_m

Surface pressures were used to calculate the sectional lift and pitching moment coefficients. Eighty-three (42 upper and 41 lower) external surface pressure taps were located at the centerline (y/b = 0.5) of the airfoil, not including the trailing-edge. Each interchangeable trailing-edge had 19 surface static pressure taps. The sectional lift coefficient and quarter-chord pitching moment coefficient were obtained by integrating the upper and lower-surface pressures at y/b = 0.5; Eq. (1) and Eq. (2). Note that only the normal force contribution is included. The axial force contribution to C_l and C_m was negligible for the 's used during the test.

$$C_l = \int_0^1 \left(C_{p_l} - C_{p_u}\right) d\left(\frac{x}{c}\right) \cos \propto \tag{1}$$

$$C_m = \int_0^1 \left(C_{p_l} - C_{p_u}\right)\left(0.25 - \left(\frac{x}{c}\right)\right) d\left(\frac{x}{c}\right) \tag{2}$$

B. Momentum Coefficient, C_μ

The jet momentum was the primary control mechanism for the experiments. To calculate the momentum coefficient, the following parameters were required: the freestream static pressure (p), the total pressure of the jet ($p_{o_{jet}}$), the total temperature of the jet ($T_{o_{jet}}$), and the mass flow rate ($\dot{m}$). Five total pressure probes in each plenum were located downstream of the high loss screens. These five pressures were averaged together to obtain the jet total pressure. A total temperature probe was also installed in each plenum at this chordwise station. The mass flow was found from the critical-flow Venturi meters installed in each air-supply line. The jet velocity calculation shown in

Eq. (3) assumes that the jet flow expands isentropically to the freestream static pressure.[24] This is the commonly accepted method for calculating the jet velocity. The momentum coefficient was then calculated using Eq. (4).

$$U_{jet} = \sqrt{2 \cdot R \cdot T_{o_{jet}} \cdot \left(\frac{\gamma}{\gamma-1}\right)\left[1 - \left(\frac{p_\infty}{p_{o_{jet}}}\right)^{\frac{\gamma-1}{\gamma}}\right]} \tag{3}$$

$$C_\mu = \left(\frac{\dot{m} \cdot U_{jet}}{q_\infty \cdot S}\right) \tag{4}$$

Note that C values calculated at M = 0.3 are considerably larger than C values found at M = 0.8. This is due to the dynamic pressure term in the denominator of Eq. 4. Dynamic pressure is a function of Mach number squared. Therefore, the dynamic pressure difference between M = 0.3 and M = 0.8 is a factor of $(0.8/0.3)^2$, or about 7.1, for the same static pressure. This means that, for all other terms being the same, an increase in Mach number from 0.3 to 0.8 will result in C values that are about one seventh as large.

C. Sectional Drag Coefficient, C_d

The sectional drag coefficient was found by using a wake rake. The rake was 48 inches tall and was located 30 inches (one reference chord length) from the reference airfoil trailing-edge. The wake rake had 79 total pressure and 8 static pressure taps. The distribution of total pressure probes was such that the highest concentration of probes occurred at z = 0, with probes reaching as high as 29.7 inches and down to -17.7 inches. The total and static pressure distributions in the model wake at y/b = 0.5 were then used to calculate the sectional drag coefficient using the procedure of Baals and Mourhess.[25] However, this method assumes that the entire mass flow passing out of the control volume at the plane of the rake originated from upstream at the freestream velocity (V_∞). Therefore the assumed momentum of the jet mass flow entering the control volume is $\dot{m} \cdot V_\infty$. Also, note that the drag calculation is a measure of momentum deficit, meaning that the upstream momentum has a positive sign. This is important in assigning the appropriate sign to the correction. The assumed upstream momentum must be subtracted back out in order to obtain the correct drag coefficient for the present experiment. The C_d in Eq. (5) is equivalent to what a balance would measure (thrust included). See Ref. 26 for a good discussion on this drag calculation technique and for other forms of C_d that account for thrust and ram effects.[26] Note that p_n and p_{o_n} are the static and total pressures, respectively, at position n.

$$C_d = C_{d_{rake}} - \left(\frac{\dot{m} \cdot V_\infty}{q_\infty \cdot S}\right) = C_{d_{rake}} - C_\mu \cdot \left(\frac{V_\infty}{U_{jet}}\right) \tag{5}$$

Where $C_{d_{rake}}$ is defined as

$$C_{d_{rake}} = \sum_{n=1}^{m} \Delta h_n \left[2\left(\frac{p_n}{p_\infty}\right)^{6/7}\left[\frac{\left(\frac{p_{o_n}}{p_n}\right)^{2/7}-1}{\left(\frac{p_{o_\infty}}{p_\infty}\right)^{2/7}-1}\right]^{1/2}\left\{\left(\frac{p_{o_n}}{p_{o_\infty}}\right)^{1/7} - \left[\frac{\left(\frac{p_{o_n}}{p_\infty}\right)^{2/7}-1}{\left(\frac{p_{o_\infty}}{p_\infty}\right)^{2/7}-1}\right]^{1/2}\right\}\right] \tag{6}$$

D. Uncertainty

The uncertainty in the calculated coefficients is a function of the freestream dynamic pressure, the pressure measurement system accuracy and the distribution of pressure taps. The uncertainty in the coefficients increased as dynamic pressure decreased because of the small differential pressures encountered at these conditions. Dynamic pressure decreased with Mach number for these tests. The uncertainty in the coefficients also increased when there were temperature differences between what was experienced during the pressure transducer calibration period and the time that the test points were collected. These characteristics were a function of the pressure transducers, the measurement system used, and the way the wind tunnel was operated. For example, the transducer calibrations had to be done at atmospheric pressure and the runs were made at sub-atmospheric pressures. One hour between calibration and data acquisition was not unusual. In addition to these factors, all coefficients were also impacted by the distribution of pressure taps, especially C_d. C_l and C_m were impacted the most when shocks were present over the upper surface in areas where the density of pressure taps was coarse. The distribution of rake-wake probes had an increasing impact on C_d as C_l increased. This was due to the fact that the pitot probes on the stationary drag rake

were concentrated at the center of the rake and then grew less dense toward the ends of the rake. At higher lift coefficients, the airfoil wake moved away from the center of the rake and into the regions of more widely spaced probes, decreasing the measurement accuracy.

The uncertainty of the coefficients has not been quantified. The results presented here use incremental lift, drag, and pitching moment coefficients. Using incremental coefficients aids in the performance evaluations considerably by decreasing the amount of bias error observed in the data. However, uncertainty in the data is still apparent by the presence of sudden unexpected jumps and general randomness found in the plots.

IV. Configurations

Four characteristics of the circulation-control airfoil model were varied during the three wind-tunnel tests. The four characteristics were 1) slot height, 2) trailing-edge design, 3) leading-edge shape, and 4) airfoil thickness. The effects of slot height, thickness, and jet or pneumatic flaps are not presented in this report. The trailing-edge design was the most widely varied characteristic. For elliptical trailing-edge aspect ratios, the radius of curvature near the slot increases with aspect ratio. However, the radius of curvature at the trailing edge decreases with aspect ratio. For the biconvex trailing-edge geometry, the radius of curvature increases with aspect ratio.

A. Trailing-Edge Geometry Variations

Four elliptical trailing-edge surfaces; referred to as Coanda trailing-edge geometries, were manufactured with major-axis to minor-axis ratios of 1.8:1, 2.4:1, 3.0:1, and 4.2:1 as illustrated in Fig. 2. The minor-axis of the Coanda surface was aligned with the slot exit, $x/c_{ref} = 0.9$. The horizontal axis of the ellipse was mapped to the camber line of the elliptical airfoil. The Coanda surface spanned the entire model (60 inches).

The three biconvex trailing-edge geometries shown in Fig. 3 were also investigated. The major-axis to minor-axis ratios were 2.0:1, 2.9:1, and 3.8:1. The biconvex design provides a constant radius of curvature over a longer distance compared to the tightening radius of the elliptical design. The rationale of this design is that at transonic conditions the jet flow might stay attached longer and eventually separate at a steeper angle when compared to that of the elliptical designs. However, unlike the elliptical Coanda surfaces, the biconvex design has the obvious limit that the flow, at best, can only remain attached to the point of the biconvex. For further details of the Coanda surface radii of curvature and configuration characteristics, please refer to the technical references.[23,27]

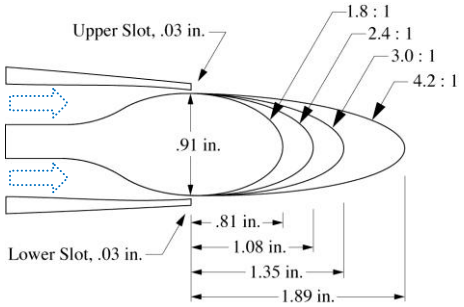

Figure 2. Elliptical Trailing-Edges

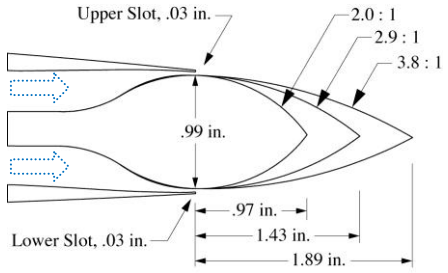

Figure 3. Biconvex Trailing-Edges

B. Leading-Edge Geometry Variations

Several leading-edge design variations were investigated. The leading-edge design of an airfoil can limit the maximum lift achievable if the leading-edge separates. Leading-edge separation can occur due to the continuing downward movement of the forward stagnation point as lift increases. It is possible for the circulation around the airfoil to be limited by the leading-edge design despite a good trailing-edge design. The three alternate leading-edge geometries are more likely to maintain attached flow by increasing the leading-edge radius and by effectively increasing camber (i.e. leading-edge "droop"). The four leading-edge designs that were tested are shown in Fig. 4.

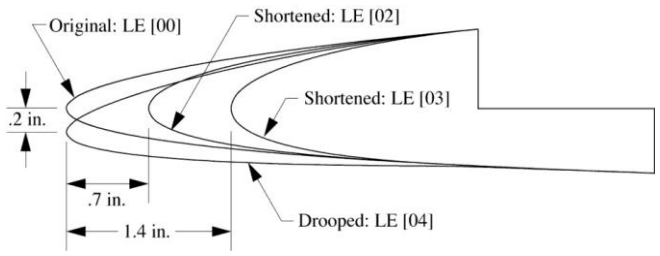

Figure 4. Leading-Edges.

V. Discussion of Results

The focus for this research is to see whether sufficient control power can be generated at transonic conditions with low momentum blowing. From a system point of view, it is important to note that substantial mass flow or high plenum pressures may limit the momentum coefficient operating range. The important metrics are maximum lift increment, lift augmentation, and net drag increment benefit. Maximum lift increment is important for evaluating maximum control power that can be achieved. Lift augmentation is important because it is desired that control power is achieved efficiently. Lift augmentation is the ratio of lift increment versus momentum coefficient. It is the initial slope of each curve found on the lift increment versus momentum coefficient plots. Higher initial slope implies greater efficiency of the configuration. Finally, net drag increment benefit includes thrust recovery, separation control, and the ability to use drag as a yaw control device.

The transonic results are presented at M = 0.8 at a nominal cruise angle-of-attack of three degrees. Results at Mach = 0.3 at = 6° are also included for evaluation of the trade-off between low-speed versus high-speed effectiveness. Baseline airfoil performance is introduced, followed by the effects of upper and lower-surface blowing, and lastly results of leading-edge surface effects.

A. Baseline Airfoil Configurations

The baseline airfoil performance of each configuration did not vary significantly without augmentation of the flow through means of circulation-control. Examples of the baseline are shown in Fig. 5 and Fig. 6 for the different elliptical trailing-edge configurations at M = 0.3 and M = 0.8. Coefficient of lift versus angle-of-attack, coefficient of pitching moment versus angle-of-attack, and coefficient of drag versus angle-of-attack are shown.

B. Blowing Performance

The airfoil characteristics evaluated in this work include trailing-edge geometry and leading-edge geometry. Each Coanda surface at the given Mach number and angle-of-attack is capable of generating incremental lift, drag, and pitching moment at each blowing condition with the exception of dual-surface blowing. Dual-surface blowing did not create any appreciable incremental lift and pitching moments. The dual-surface blowing data show primarily whether drag reduction effects could be obtained by using the jet to eliminate separation and fill the wake that would otherwise result from the elliptical Coanda surface trailing-edges. Dual-surface blowing data results from the first test entry can be found in Ref. 23.

Increasing momentum coefficient during upper slot blowing creates positive lift increments and negative pitching moment increments; for example Fig. 7b. Conversely, increasing momentum coefficient during lower slot blowing creates negative lift and positive pitching moment increments; for example Fig. 8b. Effectiveness of the Coanda configurations and net benefit of lift augmentation at subsonic Mach numbers often continues at higher momentum coefficients. Effectiveness of the Coanda configurations and net benefit of lift augmentation at transonic Mach numbers often decreases at higher momentum coefficients as a result of jet sheet detachment and consequent separation point movement. For example, this effect is visible in Fig. 9b at the point where no corresponding lift is achieved with additional blowing. At M = 0.8, overall lift, drag, and pitching moment increments for circulation-control configurations are generally less when compared to subsonic Mach numbers. Transonic lift increments are roughly half of the subsonic lift increments. This can be attributed to the decreased pressure gradient across the separating jet. The pressure gradient is a function of the velocity ratio between the freestream velocity and the jet velocity. This velocity ratio between the Coanda jet and the freestream is important. Velocity ratio is directly related to the lower pressure on surface of the Coanda geometry that maintains jet attachment. The Coanda jet detachment location determines the location of the stagnation point and therefore the circulation around the airfoil. Within limits, the higher the velocity ratio, the smaller the Coanda radius that the Coanda jet can remain attached to. At transonic conditions this ratio decreases and thus the larger and gentler sloping Coanda surfaces generally performed better. To generate appreciable lift increment benefits at transonic Mach number, the corresponding momentum coefficients are significantly less because of the dependence of C on dynamic pressure. Again, the primary factor is where the stagnation point is set: the farther around the surface, the higher the circulation around the airfoil and thus the higher the lift.

C. Trailing-Edge Surface Effect

1. Elliptical Trailing-Edge Performance

Aerodynamic characteristics at Mach = 0.3, = 6°, of upper-surface and lower-surface blowing over elliptical Coanda surfaces [1.8:1], [2.4:1], [3.0:1] and [4.2:1] are shown in Fig. 7 and 8. Figure 7b shows how the incremental lift performance clearly deteriorated for the largest aspect ratio surface. The elliptical Coanda geometry [1.8:1]

resulted in the best lift augmentation and the highest overall lift and drag increment characteristics, achieving a C_l ~ 0.675 at C ~ 0.05. There is a plateau in lift contribution that decreases with elliptical Coanda geometry aspect ratio seen in Fig. 7b. This plateau is not well understood. It is hypothesized that the dip occurs for the shorter Coanda surfaces due to the flow separating prematurely because the jet sheet reached a tighter radius of curvature sooner for the same surface distance traveled compared to the longer Coanda surfaces. Afterwards, increasing jet momentum was still able to eventually increase lift due to the jet-flap effect. There is also some unexplained behavior in the drag curve in Fig. 7c at low momentum coefficients for the [1.8:1] geometry. The drag behavior is the same for all Coanda surfaces except [1.8:1]. This implies that the wake filling and thrust is approximately equivalent for the three geometries, despite the differences in the lift increment performance. The pitching moment increment behaves very similarly to lift increment (linear relationship behavior between lift and pitching moment). The curve in Fig. 7b shows negative moment with increasing blowing which is explainable by the increasing suction at the trailing-edge observed in Fig. 7a.

During lower-surface blowing at Mach = 0.3 the general behavior of each trailing-edge Coanda surface is very similar to what was found for upper-surface blowing (Fig. 8). The elliptical Coanda geometry [1.8:1] performs best by achieving a higher lift increment with less blowing compared to the other configurations (Fig. 8b). For example, it achieves the largest lift increment, C_l ~ -0.7, at a moderate momentum coefficient, C ~ 0.4. As found with upper-surface blowing, lower-surface blowing results show that configuration [4.2:1] has the least favorable characteristics. Also similar to the upper-surface blowing results, the lift increment for Coanda geometry [1.8:1] plateaus in the middle of the momentum coefficient range tested. The C_d results shown in Fig. 8c show that all configurations have very similar drag characteristics with all having very good thrust recovery. Overall, elliptical Coanda geometry [1.8:1] performed best for upper and lower surface blowing at M = 0.3. Maximum lift increment and lift augmentation decreased with increasing aspect ratio.

Aerodynamic characteristics at Mach = 0.8, = 3°, of upper-surface and lower-surface blowing over the same four elliptical Coanda configurations are shown in Fig. 9 and 10. The incremental lift performance presented in Fig. 9b shows that elliptical Coanda surface [4.2:1] achieved the highest lift increment of 0.25 at C ~ 0.011; however, it had the lowest lift augmentation (i.e. poorest efficiency). For a more modest momentum coefficient of 0.008, elliptical Coanda surface [3.0:1] performed better (C_l ~ 0.225). Coanda surface [2.4:1] performed similarly to surface [3.0:1] up to C ~ 0.006. At higher momentum coefficient, the shortest Coanda surface resulted in the poorest performance due to the Coanda jet separating from the surface earlier compared to the other geometries. The trend of longer Coanda surfaces which have larger radius of curvature performing better at higher freestream conditions is consistent with what can be found in the literature. As found in the Mach = 0.3 data, the pitching moment follows the same trends (with sign reversed) as the lift increment. The drag increment results all show a similar trend but with differences in the details of the curves. Thrust recovery is good for all geometries due to the jet providing both direct thrust and separation control over the blunt trailing-edge.

The lower-surface blowing results are shown in Fig. 10 where it can be seen that lift increments are smaller compared to upper-surface blowing results. The elliptical Coanda geometry [2.4:1] performs best during lower-surface blowing, achieving a C_l ~ -0.15 at C ~ 0.006. For upper and lower blowing, drag becomes more linear with increasing Coanda aspect ratio; as shown in Fig. 9c and Fig. 10c. Overall at M = 0.8, elliptical Coanda geometry [3.0:1] performed best for upper surface blowing and elliptical Coanda geometry [2.4:1] performed best during lower surface blowing. Two trends are visible for upper and lower surface blowing. At momentum coefficients up to C ~ 0.005, lift augmentation decreased with increasing Coanda aspect ratio. Unlike the subsonic condition, maximum lift increment increased with increasing aspect ratio.

2. Biconvex Trailing-Edge Performance

Aerodynamic characteristics at Mach = 0.3, = 6°, of upper-surface and lower-surface blowing over biconvex Coanda configurations [2.0:1], [2.9:1] and [3.8:1] are shown in Fig. 11 and 12. The leading-edge used during these test points was not the same as the leading-edge used in the elliptical Coanda surface results previously presented. As discussed in the next section, leading-edges can impact the airfoil performance. The leading-edge used for the biconvex test points shown here was the best leading-edge geometry found from the set of leading-edge geometries tested. This was leading-edge [03] which was the shortest and had the largest radius as shown in Figure 4. The results for the elliptical Coanda configuration [3.0:1] with the new leading-edge are included in the plots for comparison. As shown in Fig. 11b, the biconvex Coanda configuration [2.0:1] outperforms all other Coanda configurations presented. There is a clear trend showing that the longer the biconvex geometry, the smaller the lift increment benefit for the same C . This is expected at low freestream velocities because the jet flow is hypothetically able to reach the tip of the biconvex at these conditions, making the turning angle at the tip of the

biconvex a critical factor in the aerodynamic performance. Note that the biconvex [2.9:1] and elliptical Coanda [3.0:1] produce very similar lift increment behavior. As found for the elliptical Coanda surface, the pitching moment follows the same trends, with sign reversed, as the lift increment. The drag increment results all show a similar trend but with differences in the details of the curves. Lower-surface blowing presented in Fig. 12 show that the shortest biconvex geometry produces the largest lift and pitching moment increments. Overall, the Mach = 0.3 biconvex results show that the [2.0:1] biconvex surface had the best aerodynamic performance characteristics. For upper and lower surface blowing at M = 0.3, maximum lift increment and lift augmentation increases with decreasing Coanda surface aspect ratio.

Aerodynamic characteristics at Mach = 0.8, = 3°, of upper-surface and lower-surface blowing over the same three biconvex Coanda configurations [2.0:1], [2.9:1] and [3.8:1] are shown in Fig. 13 and 14. The Mach = 0.8 results presented in Fig. 13b show that the longest biconvex performed best and that the shortest biconvex had the poorest performance. The sharp reversal in the lift increment curve for the shortest biconvex Coanda surface indicates that the jet sheet separated. This can be attributed to the smaller radius of curvature of the shortest biconvex surface compared to the other geometries. The elliptical Coanda surface achieved the highest incremental lift value ($C_l \sim 0.28$) compared to any of the biconvex Coanda configurations, although the [3.8:1] biconvex was a very close second. It is important to note that the biconvex Coanda configurations have a higher lift increment slope than the elliptical configurations for lower momentum coefficients. They achieve a consistently higher lift increment for the same momentum coefficients less than $C_\mu \sim 0.006$. This is because of the immediate turning of the flow due to the biconvex geometry, i.e., a smaller radius of curvature near the slot compared to the elliptical geometries. As found for the elliptical Coanda surfaces, the pitching moment follows the same trends (with sign reversed) as the lift increment. The drag increment results all show a similar trend but with differences in the details of the curves. The lower-surface blowing results shown in Fig. 14 show that the lift and pitching moment increment behavior is similar to that for upper-surface blowing but with lower absolute magnitudes. Overall, the Mach = 0.8 biconvex results show that the [3.8:1] biconvex surface had the best performance ($C_\mu < 0.006$), and comes very close to matching the maximum lift increment ($C_l \sim 0.28$) achieved by the [3.0:1] elliptical surface.

D. Leading-Edge Surface Effect

Aerodynamic characteristics of upper-surface and lower-surface blowing over elliptical Coanda trailing-edge [3.0:1] and four leading-edge geometries are shown in Figs. 15-18. At Mach = 0.3, = 6°, leading-edge geometry [03] provided the best lift ($C_l \sim 0.66$) and drag ($C_d \sim -0.045$) increment performance at momentum coefficient $C_\mu \sim 0.06$. Note that the target C_μ of 0.06 was selected somewhat arbitrarily and is meant to serve as a comparison point for discussion purposes. Leading-edge performance is readily observed in Fig. 15a by examining the pressure coefficient peaks that occur in the first 5% chord. The low suction peak of leading-edges [00] and [02] are a result of separation occurring on the leading-edge. The "drooped" leading-edge [04] performs better, presumably because it reduces the angle that the airfoil sees with respect to the freestream and effectively increases camber. Lastly, leading-edge [03] attains the highest C_p peak (as a result of leading-edge radius), indicating that it had the least amount of separation, if any. Not surprisingly, the aerodynamic characteristics shown in Fig. 15b and 15c reveal that leading-edge [03] resulted in the most desirable behavior. The lower-surface blowing results shown in Fig. 16 show that leading-edge geometry changes did not significantly impact aerodynamic performance at Mach = 0.3, 6°.

At Mach = 0.8, = 3°, leading-edge configurations [02], [03] and [04] result in better lift increment characteristics than the baseline leading-edge design (Fig. 17). All three alternate designs share very similar behavior and obtain the same maximum lift increment of $C_l \sim 0.275$ at $C_\mu \sim 0.0085$. This shows that the three leading-edge designs were sufficient to improve the aerodynamic characteristics over the baseline design [00] but that sensitivity to a particular design has largely disappeared. It is hypothesized that other factors such as compressibility and flow physics at the trailing-edge become more important in attaining higher lift increments at the Mach = 0.8 condition. Although the three alternate leading-edge designs result in the same lift-increment behavior, there are differences in the pressure field over the upper-surface of the airfoil (Fig. 17a). Evidence of an upper-surface shock is most clearly seen with leading-edge configuration [03]. This leading-edge had the largest radius and therefore supported the greatest flow acceleration. The shock becomes progressively weaker and moves forward as the leading-edge radius becomes smaller. The data shown in Fig. 17b and 17c indicate that the jet flow along the Coanda surface separates early or is "blown off" due to the large amount of blowing at this C_μ. Figure 17b shows this by the way the lift increment peaks and then starts to fall off above $C_\mu \sim 0.008$, indicating that the aft stagnation point movement reversed direction. Figure 17c shows this by the presence of the drag rise at the same C_μ. Lower-surface blowing results shown in Fig. 18 show similar behavior as upper-surface blowing but with decreased

magnitudes in the aerodynamic increments. Unlike the Mach = 0.3 results, the drag increment behavior at Mach = 0.8 exhibits an abrupt upward turn as shown in Figs. 17c (C_μ ~ 0.004), and 18c (C_μ ~ 0.008). Although the effectiveness of each configuration is not nearly as sensitive to leading-edge geometry as it is to trailing-edge geometry; the best leading-edge geometry is leading-edge [03]. It has the largest radius, performs best at Mach = 0.3, and is one of the best performers at Mach = 0.8.

VI. Conclusion

Wind-tunnel tests were conducted in the NASA Langley Transonic Dynamics Tunnel on a 6 percent-thick, elliptical circulation-control airfoil with upper-surface and lower-surface blowing capability. Elliptical Coanda trailing-edge geometries, biconvex Coanda trailing-edge geometries, and leading-edge geometries are presented at subsonic and transonic Mach numbers of 0.3 and 0.8, respectively. The focus of this investigation was to see how effectively circulation control could be used to generate control power at transonic conditions using upper and/or lower surface blowing.

At M = 0.3, = 6, decreasing the aspect ratio of the elliptical or biconvex trailing edges increases the maximum lift increment and the lift augmentation ratio. For both geometry types, the smallest aspect ratio, and therefore the smallest radius of curvature, resulted in the best aerodynamic performance.

At M = 0.8, = 3, maximum lift increment is roughly half of the M = 0.3 increment as a result of the lower freestream to jet velocity ratio. The available blowing coefficient range at M = 0.8 is also much less due to the inverse dependence of C_μ on dynamic pressure. For elliptical geometries, the [2.4:1] and [3.0:1] trailing edges provided the best aerodynamic performance at M = 0.8. Decreasing the aspect ratio of Coanda geometries reduces maximum lift increment and increases the lift augmentation ratio. For the biconvex geometries, the largest aspect ratio geometry [3.8:1] provided the best transonic aerodynamic performance. Smaller aspect ratio biconvex geometries resulted in early jet-sheet separation and loss of lift, analogous to the elliptical results.

Although the effectiveness of each configuration is not nearly as sensitive to leading-edge geometry as it is to trailing-edge geometry; the best leading-edge geometry is leading-edge [03]. It has the largest radius, resulted in the least amount of separated flow at Mach = 0.3, and is one of the best performers at Mach = 0.8.

It was found that the [3.0:1] ratio elliptical Coanda surface with the most rounded leading-edge [03] provided the best aerodynamic performance. This configuration generated a maximum $C_l = 0.625$ at a $C_\mu = 0.06$ at M = 0.3, = 6 . This same configuration generated a maximum $C_l = 0.275$ at a $C_\mu = 0.0085$ at M = 0.8, = 3 .

LE	TE	Description
[00]	[1.8:1]	Baseline airfoil leading-edge w/Elliptical Coanda trailing-edge [1.8:1]
[00]	[2.4:1]	Baseline airfoil leading-edge w/Elliptical Coanda trailing-edge [2.4:1]
[00]	[3.0:1]	Baseline airfoil leading-edge w/Elliptical Coanda trailing-edge [3.0:1]
[00]	[4.2:1]	Baseline airfoil leading-edge w/Elliptical Coanda trailing-edge [4.2:1]

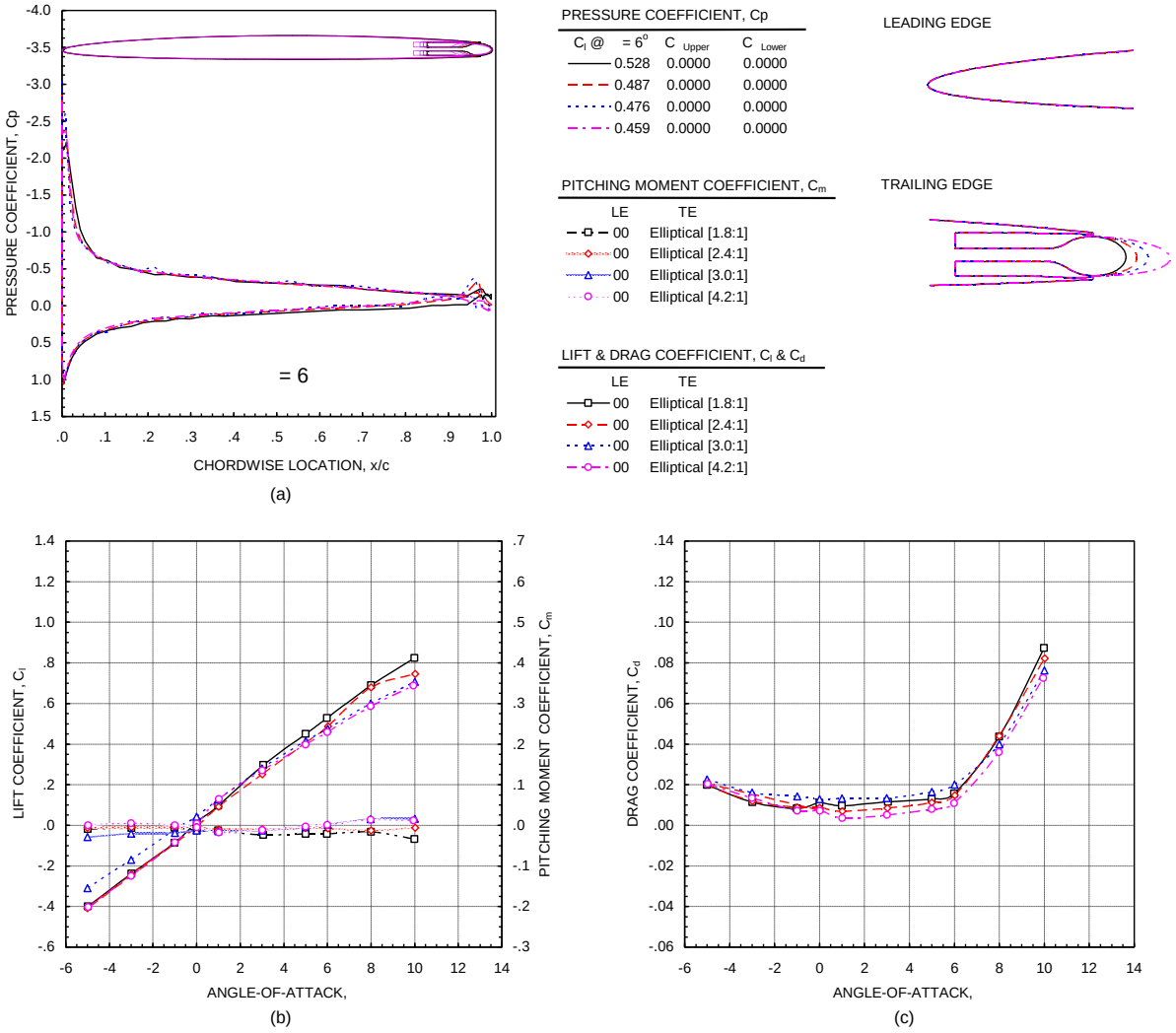

Figure 5. Airfoil performance at M = 0.3, for zero-blowing cases for elliptical trailing-edge geometry variations.

LE	TE	Description
[00]	[1.8:1]	Baseline airfoil leading-edge w/Elliptical Coanda trailing-edge [1.8:1]
[00]	[2.4:1]	Baseline airfoil leading-edge w/Elliptical Coanda trailing-edge [2.4:1]
[00]	[3.0:1]	Baseline airfoil leading-edge w/Elliptical Coanda trailing-edge [3.0:1]
[00]	[4.2:1]	Baseline airfoil leading-edge w/Elliptical Coanda trailing-edge [4.2:1]

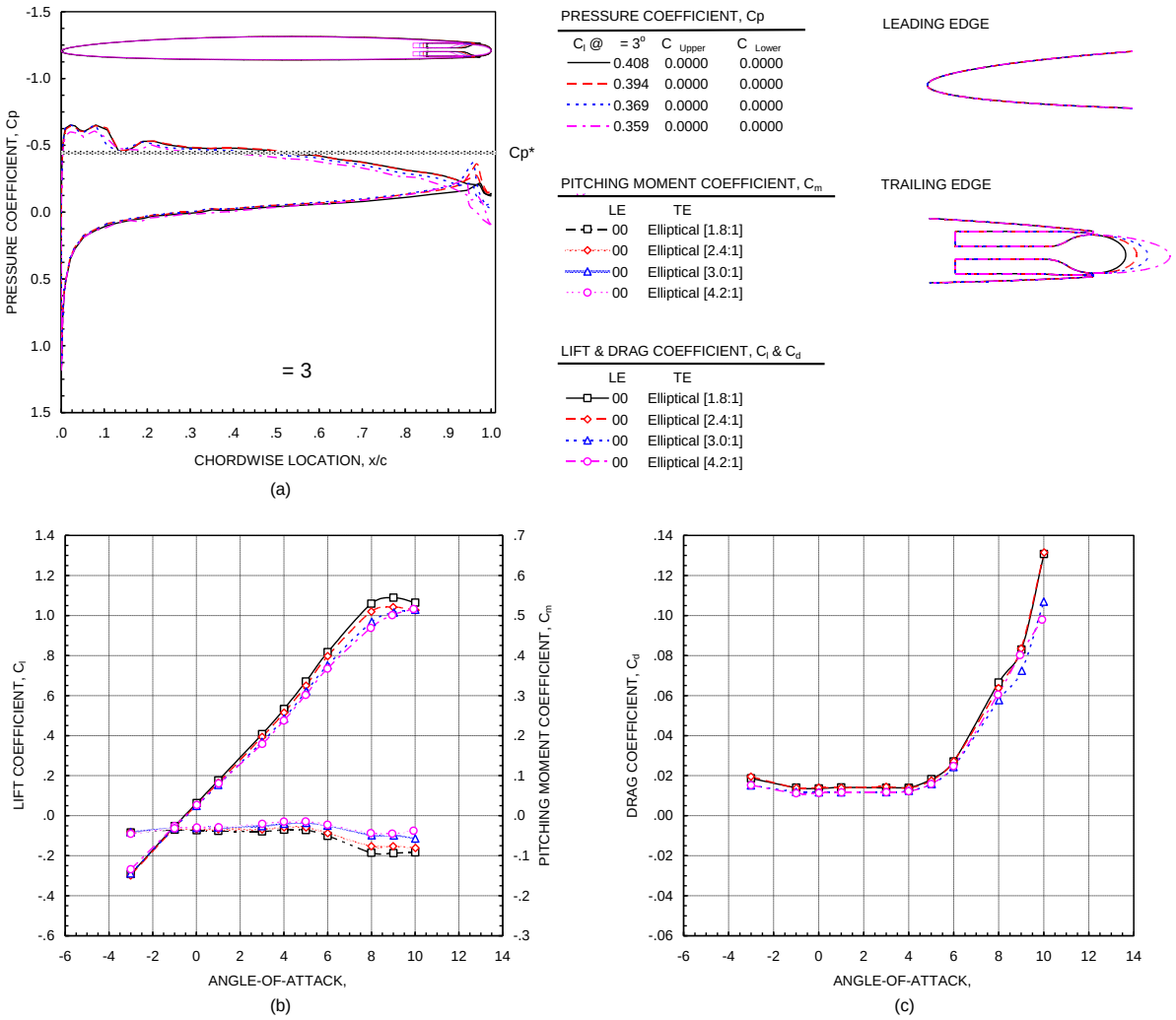

Figure 6. Airfoil performance at M = 0.8, for zero-blowing cases for elliptical trailing-edge geometry variations.

LE	TE	Description
[00]	[1.8:1]	Baseline airfoil leading-edge w/Elliptical Coanda trailing-edge [1.8:1]
[00]	[2.4:1]	Baseline airfoil leading-edge w/Elliptical Coanda trailing-edge [2.4:1]
[00]	[3.0:1]	Baseline airfoil leading-edge w/Elliptical Coanda trailing-edge [3.0:1]
[00]	[4.2:1]	Baseline airfoil leading-edge w/Elliptical Coanda trailing-edge [4.2:1]

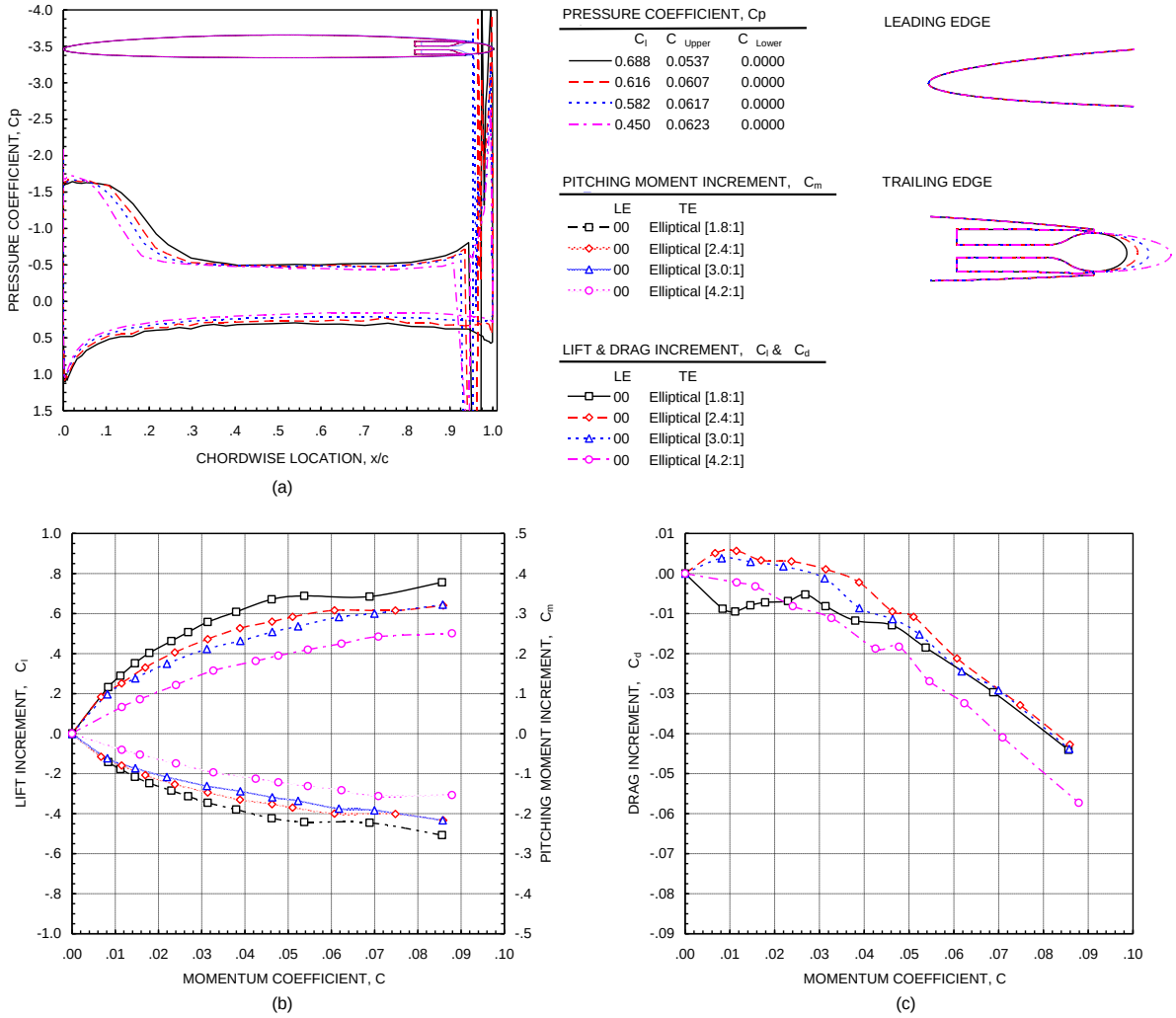

Figure 7. Airfoil performance at M = 0.3, = 6 , for upper-surface blowing for elliptical Coanda trailing-edge geometries.

LE	TE	Description
[00]	[1.8:1]	Baseline airfoil leading-edge w/Elliptical Coanda trailing-edge [1.8:1]
[00]	[2.4:1]	Baseline airfoil leading-edge w/Elliptical Coanda trailing-edge [2.4:1]
[00]	[3.0:1]	Baseline airfoil leading-edge w/Elliptical Coanda trailing-edge [3.0:1]
[00]	[4.2:1]	Baseline airfoil leading-edge w/Elliptical Coanda trailing-edge [4.2:1]

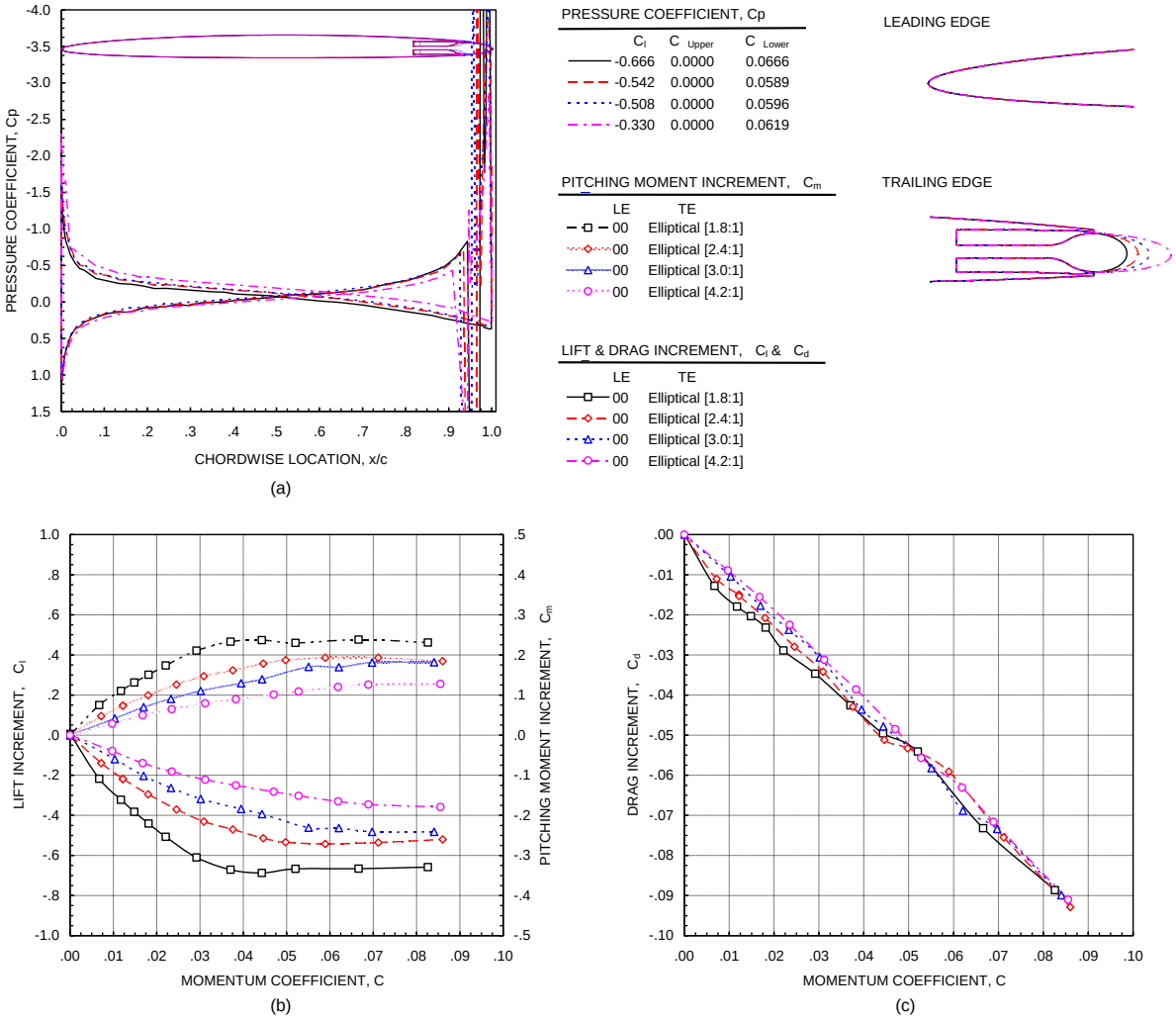

Figure 8. Airfoil performance at M = 0.3, = 6 , for lower-surface blowing for elliptical Coanda trailing-edge geometries.

LE	TE	Description
[00]	[1.8:1]	Baseline airfoil leading-edge w/Elliptical Coanda trailing-edge [1.8:1]
[00]	[2.4:1]	Baseline airfoil leading-edge w/Elliptical Coanda trailing-edge [2.4:1]
[00]	[3.0:1]	Baseline airfoil leading-edge w/Elliptical Coanda trailing-edge [3.0:1]
[00]	[4.2:1]	Baseline airfoil leading-edge w/Elliptical Coanda trailing-edge [4.2:1]

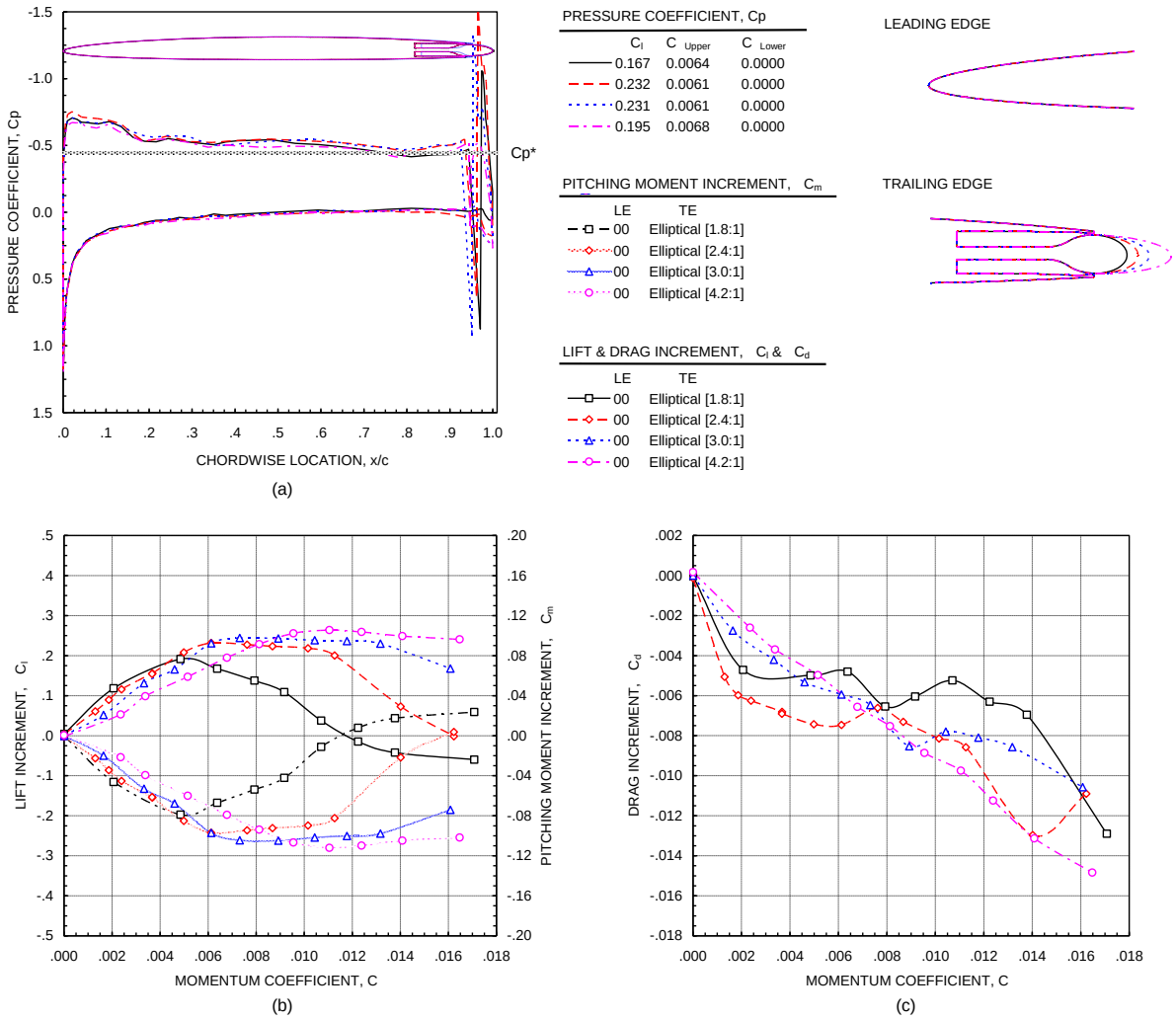

Figure 9. Airfoil performance at M = 0.8, = 3 , for upper-surface blowing for elliptical Coanda trailing-edge geometries.

LE	TE	Description
[00]	[1.8:1]	Baseline airfoil leading-edge w/Elliptical Coanda trailing-edge [1.8:1]
[00]	[2.4:1]	Baseline airfoil leading-edge w/Elliptical Coanda trailing-edge [2.4:1]
[00]	[3.0:1]	Baseline airfoil leading-edge w/Elliptical Coanda trailing-edge [3.0:1]
[00]	[4.2:1]	Baseline airfoil leading-edge w/Elliptical Coanda trailing-edge [4.2:1]

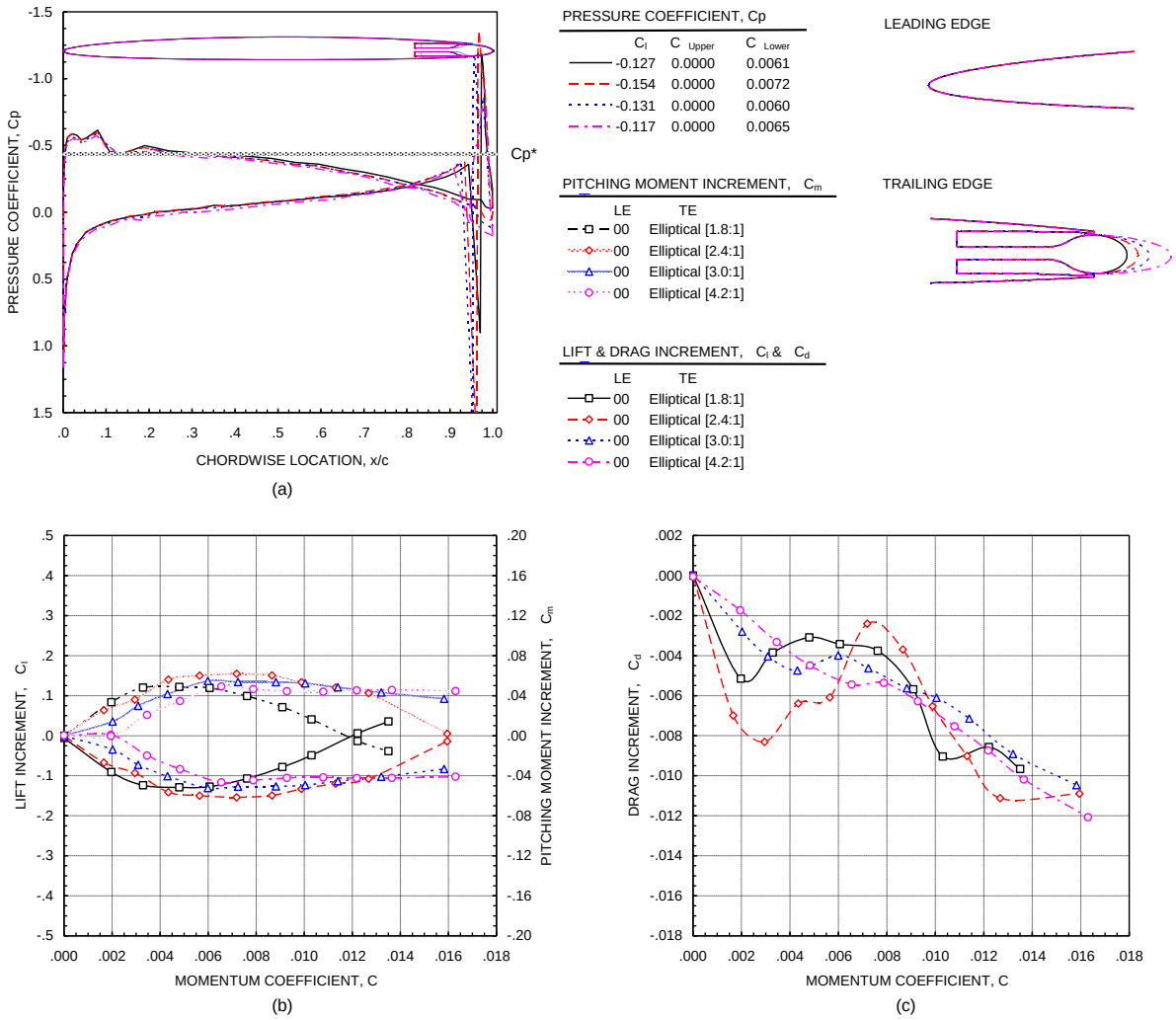

Figure 10. Airfoil performance at M = 0.8, = 3 , for lower-surface blowing for elliptical Coanda trailing-edge geometries.

LE	TE	Description
[03]	[3.0:1]	Shortest, largest LE radius w/Elliptical Coanda TE [3.0:1]
[03]	[2.0:1]	Shortest, largest LE radius w/Biconvex Coanda trailing-edge [2.0:1]
[03]	[2.9:1]	Shortest, largest LE radius w/Biconvex Coanda trailing-edge [2.9:1]
[03]	[3.8:1]	Shortest, largest LE radius w/Biconvex Coanda trailing-edge [3.8:1]

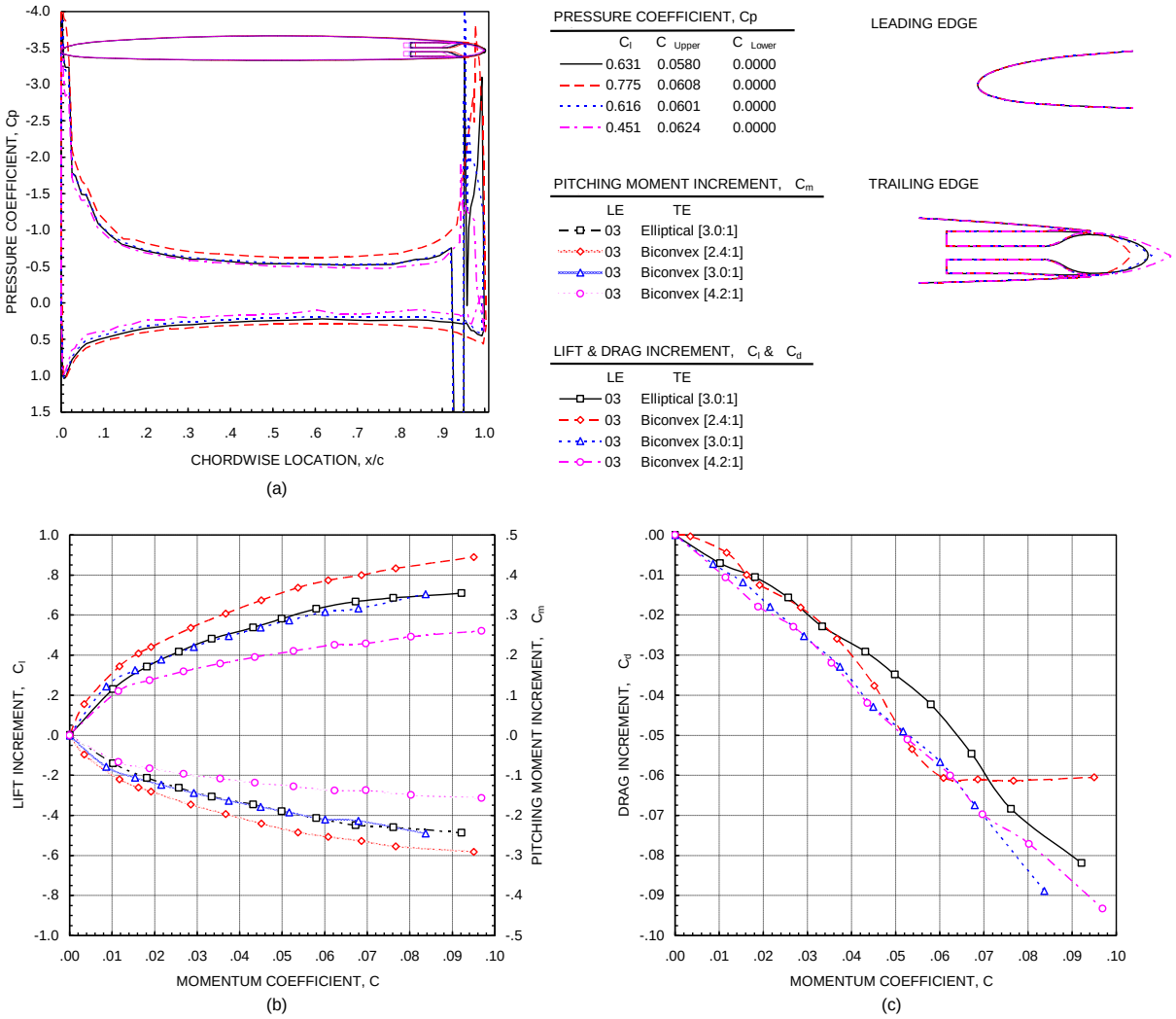

Figure 11. Airfoil performance at M = 0.3, = 6 , for upper-surface blowing for biconvex Coanda trailing-edge geometries.

LE	TE	Description
[03]	[3.0:1]	Shortest, largest LE radius w/Elliptical Coanda TE [3.0:1]
[03]	[2.0:1]	Shortest, largest LE radius w/Biconvex Coanda trailing-edge [2.0:1]
[03]	[2.9:1]	Shortest, largest LE radius w/Biconvex Coanda trailing-edge [2.9:1]
[03]	[3.8:1]	Shortest, largest LE radius w/Biconvex Coanda trailing-edge [3.8:1]

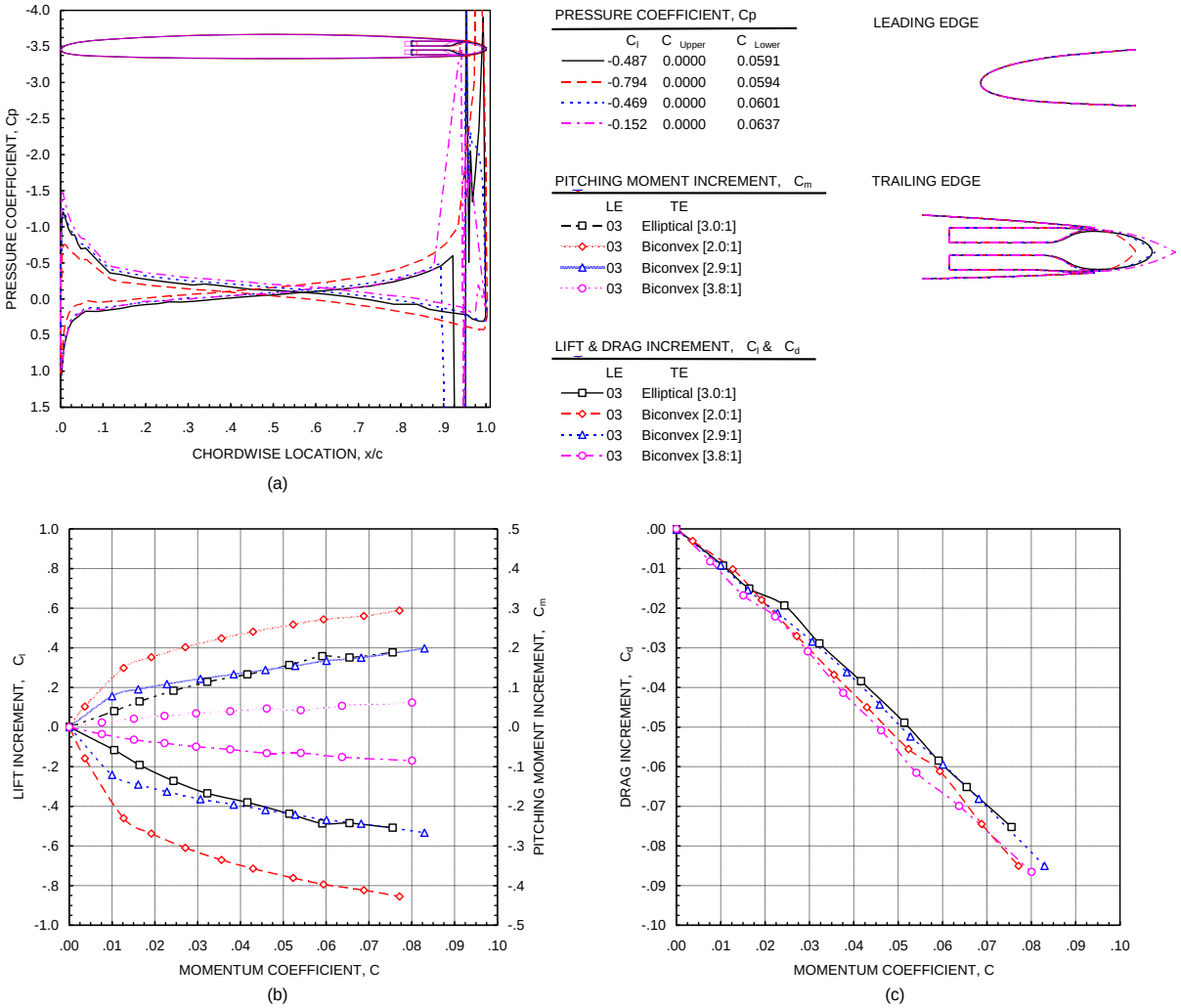

Figure 12. Airfoil performance at M = 0.3, = 6 , for lower-surface blowing for biconvex Coanda trailing-edge geometries.

LE	TE	Description
[03]	[3.0:1]	Shortest, largest LE radius w/Elliptical Coanda TE [3.0:1]
[03]	[2.0:1]	Shortest, largest LE radius w/Biconvex Coanda trailing-edge [2.0:1]
[03]	[2.9:1]	Shortest, largest LE radius w/Biconvex Coanda trailing-edge [2.9:1]
[03]	[3.8:1]	Shortest, largest LE radius w/Biconvex Coanda trailing-edge [3.8:1]

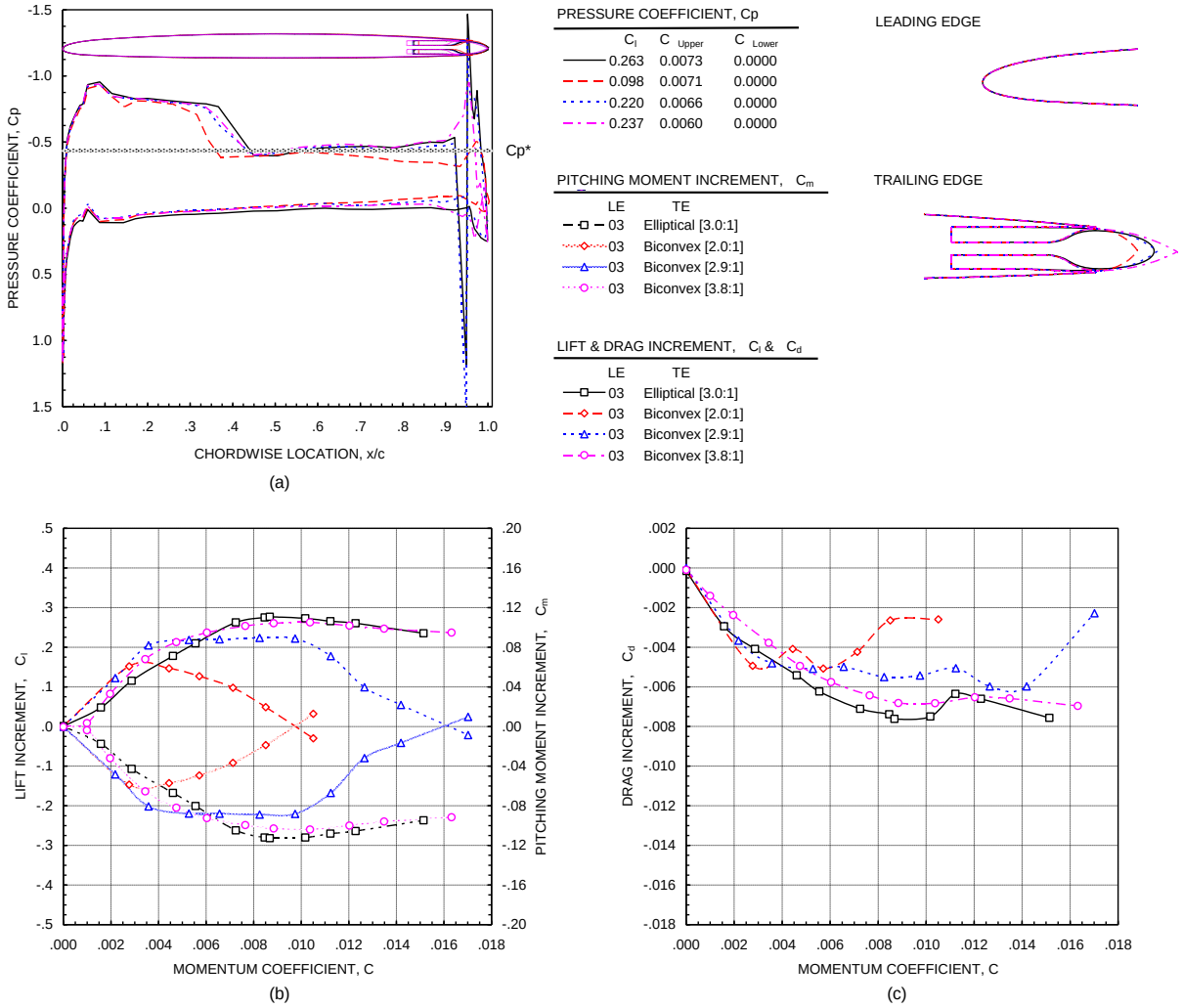

Figure 13. Airfoil performance at M = 0.8, = 3 , for upper-surface blowing for biconvex Coanda trailing-edge geometries.

LE	TE	Description
[03]	[3.0:1]	Shortest, largest LE radius w/Elliptical Coanda TE [3.0:1]
[03]	[2.0:1]	Shortest, largest LE radius w/Biconvex Coanda trailing-edge [2.0:1]
[03]	[2.9:1]	Shortest, largest LE radius w/Biconvex Coanda trailing-edge [2.9:1]
[03]	[3.8:1]	Shortest, largest LE radius w/Biconvex Coanda trailing-edge [3.8:1]

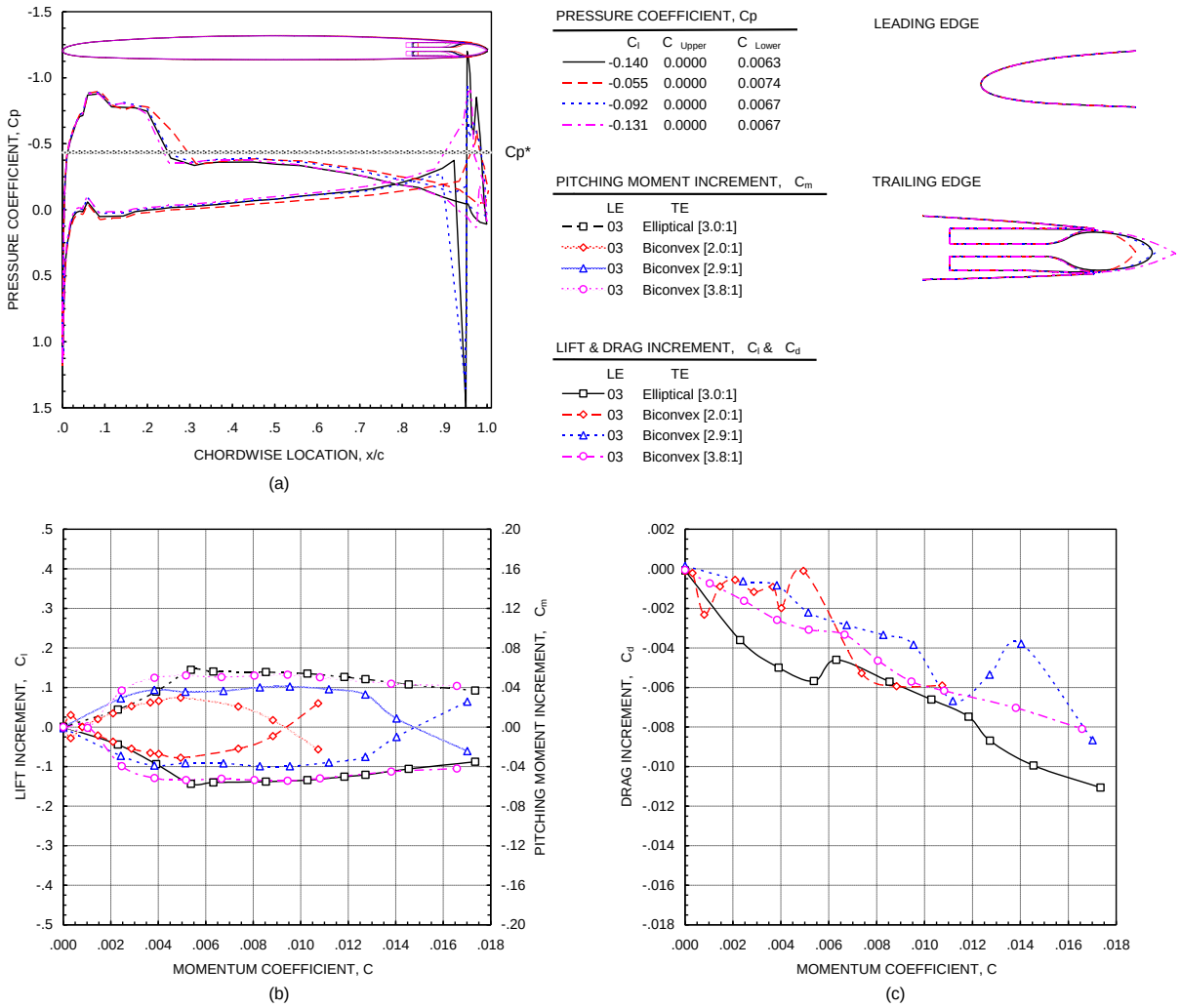

Figure 14. Airfoil performance at M = 0.8, = 3 , for lower-surface blowing for biconvex Coanda trailing-edge geometries.

LE	TE	Description
[00]	[3.0:1]	Original LE w/Elliptical Coanda TE [3.0:1]
[02]	[3.0:1]	Short, large LE radius w/Elliptical Coanda TE [3.0:1]
[03]	[3.0:1]	Shortest, largest LE radius w/Elliptical Coanda TE [3.0:1]
[04]	[3.0:1]	Droop LE w/Elliptical Coanda TE [3.0:1]

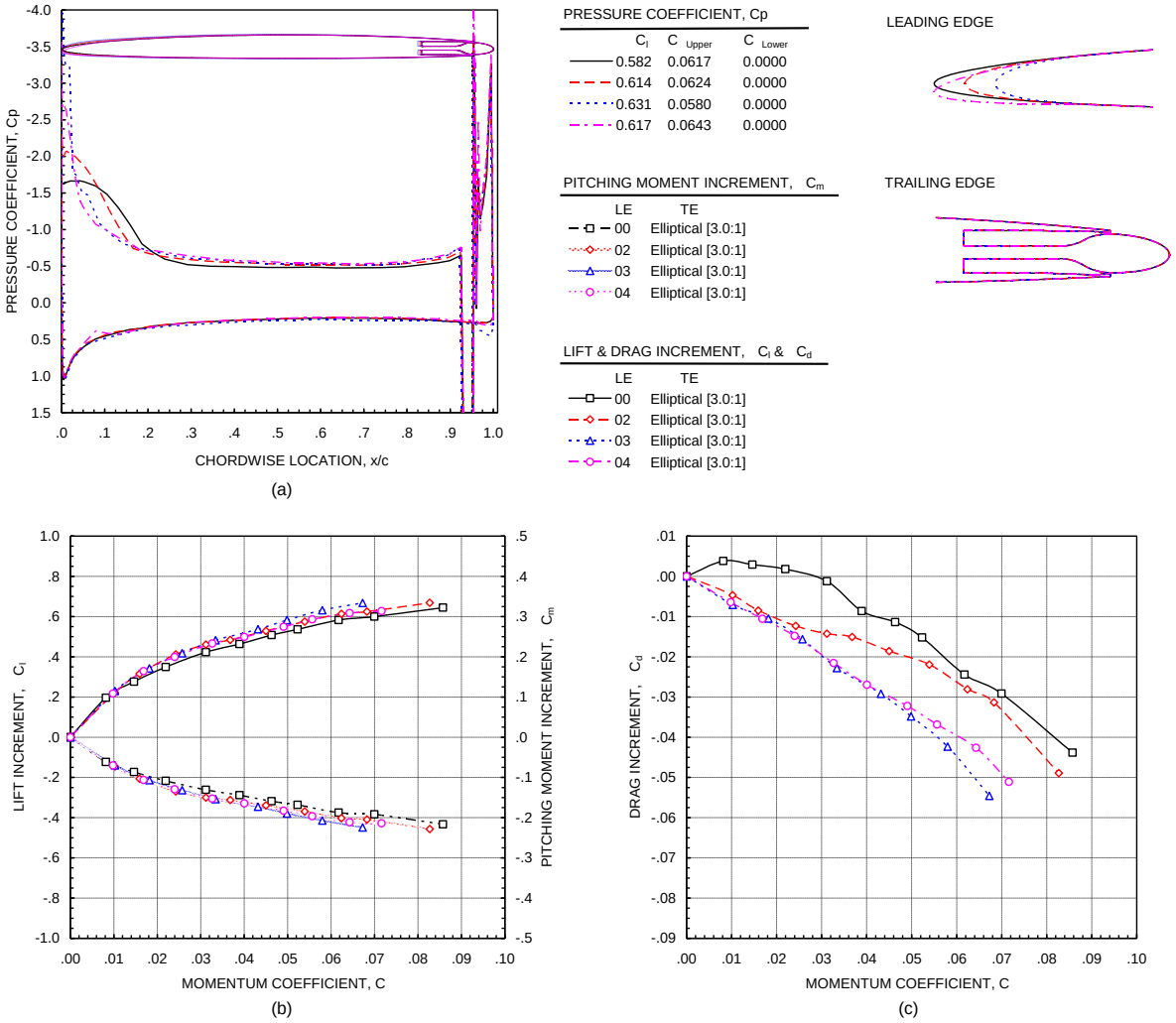

Figure 15. Airfoil performance at M = 0.3, = 6 , for upper-surface blowing for configurations having elliptical Coanda trailing-edge [3.0:1] and various leading-edge geometries.

LE	TE	Description
[00]	[3.0:1]	Original LE w/Elliptical Coanda TE [3.0:1]
[02]	[3.0:1]	Short, large LE radius w/Elliptical Coanda TE [3.0:1]
[03]	[3.0:1]	Shortest, largest LE radius w/Elliptical Coanda TE [3.0:1]
[04]	[3.0:1]	Droop LE w/Elliptical Coanda TE [3.0:1]

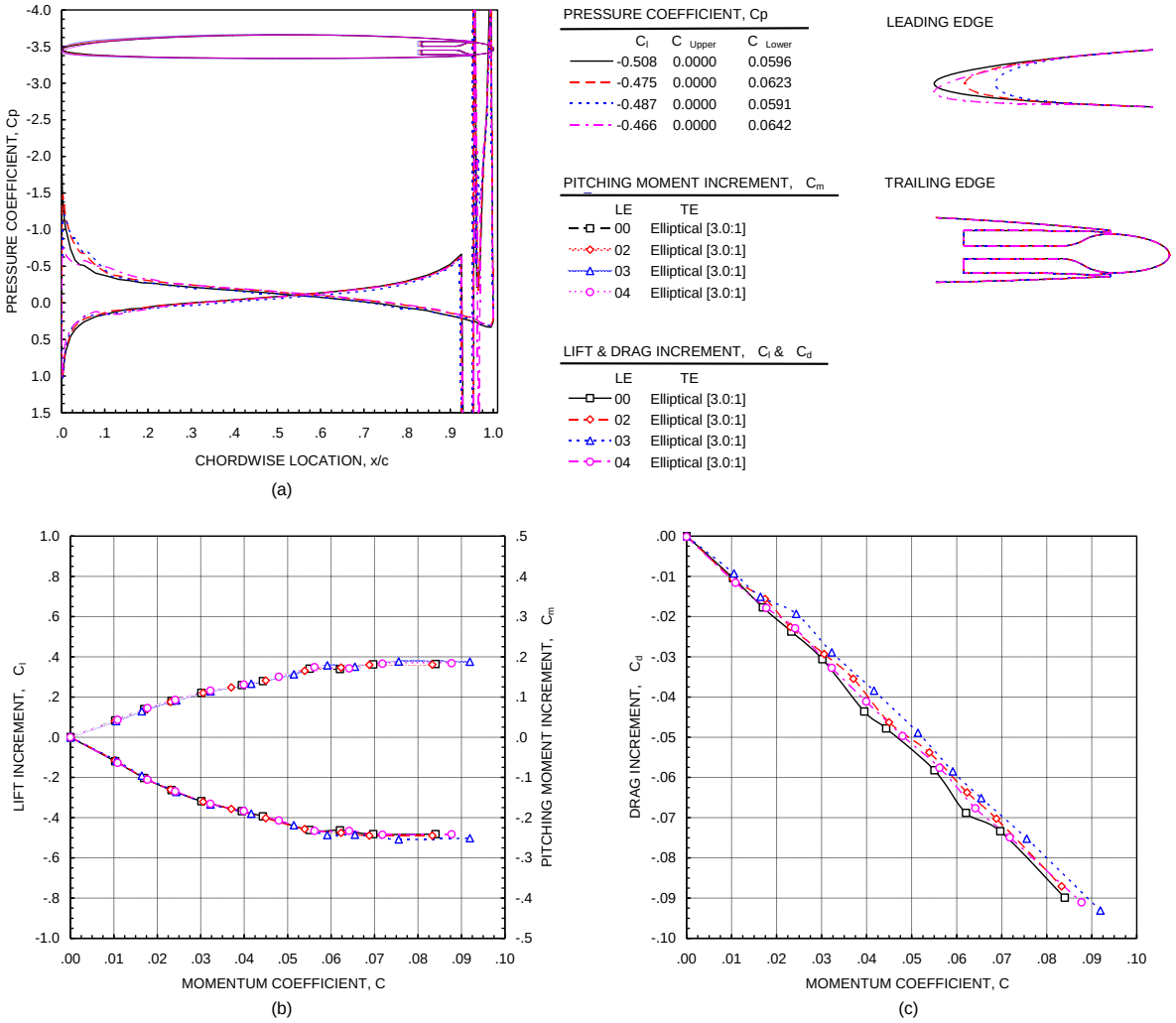

Figure 16. Airfoil performance at M = 0.3, = 6 , for lower-surface blowing for configurations having elliptical Coanda trailing-edge [3.0:1] and various leading-edge geometries.

LE	TE	Description
[00]	[3.0:1]	Original LE w/Elliptical Coanda TE [3.0:1]
[02]	[3.0:1]	Short, large LE radius w/Elliptical Coanda TE [3.0:1]
[03]	[3.0:1]	Shortest, largest LE radius w/Elliptical Coanda TE [3.0:1]
[04]	[3.0:1]	Droop LE w/Elliptical Coanda TE [3.0:1]

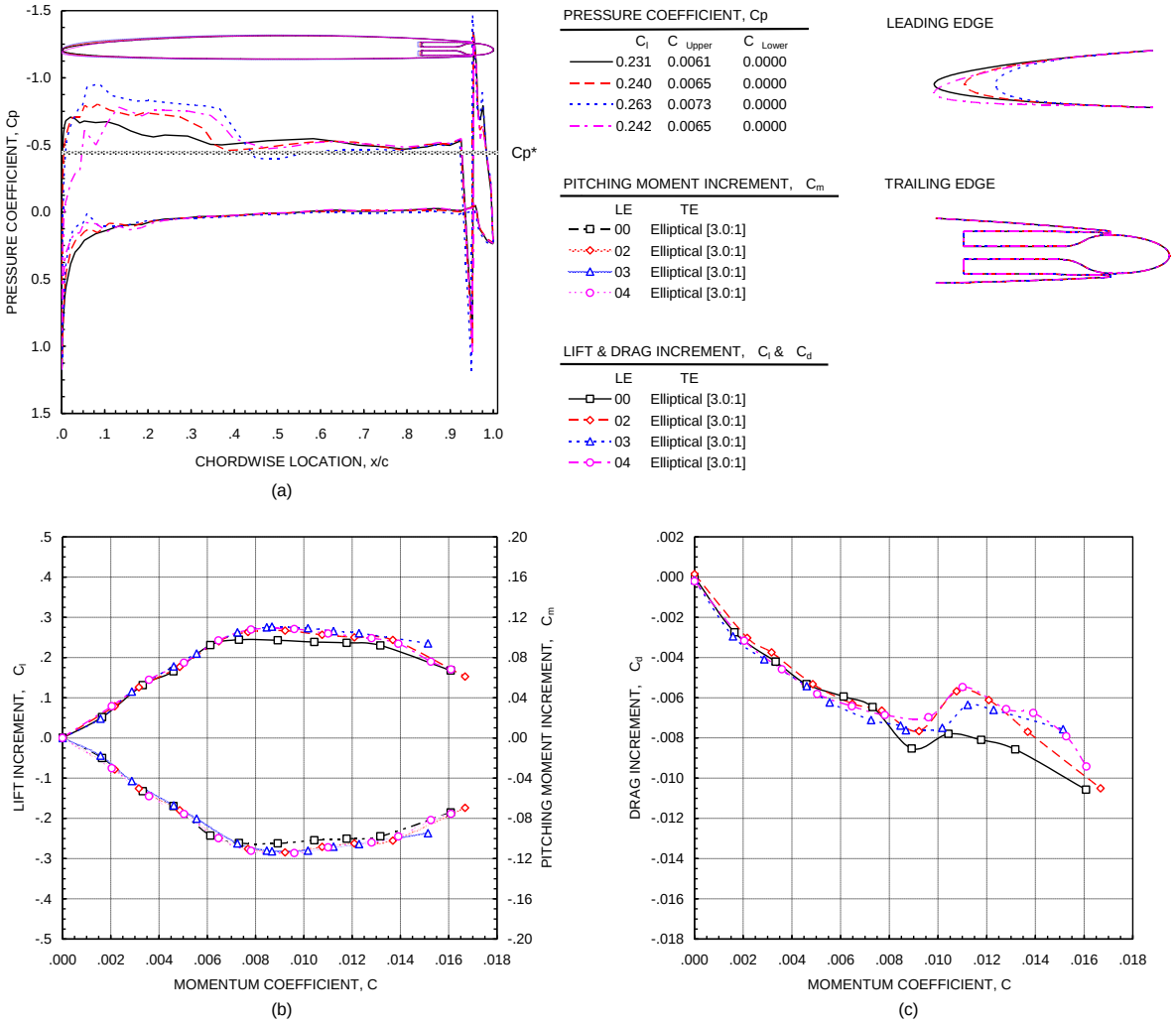

Figure 17. Airfoil performance at M = 0.8, = 3 , for upper-surface blowing for configurations having elliptical Coanda trailing-edge [3.0:1] and various leading-edge geometries.

LE	TE	Description
[00]	[3.0:1]	Original LE w/Elliptical Coanda TE [3.0:1]
[02]	[3.0:1]	Short, large LE radius w/Elliptical Coanda TE [3.0:1]
[03]	[3.0:1]	Shortest, largest LE radius w/Elliptical Coanda TE [3.0:1]
[04]	[3.0:1]	Droop LE w/Elliptical Coanda TE [3.0:1]

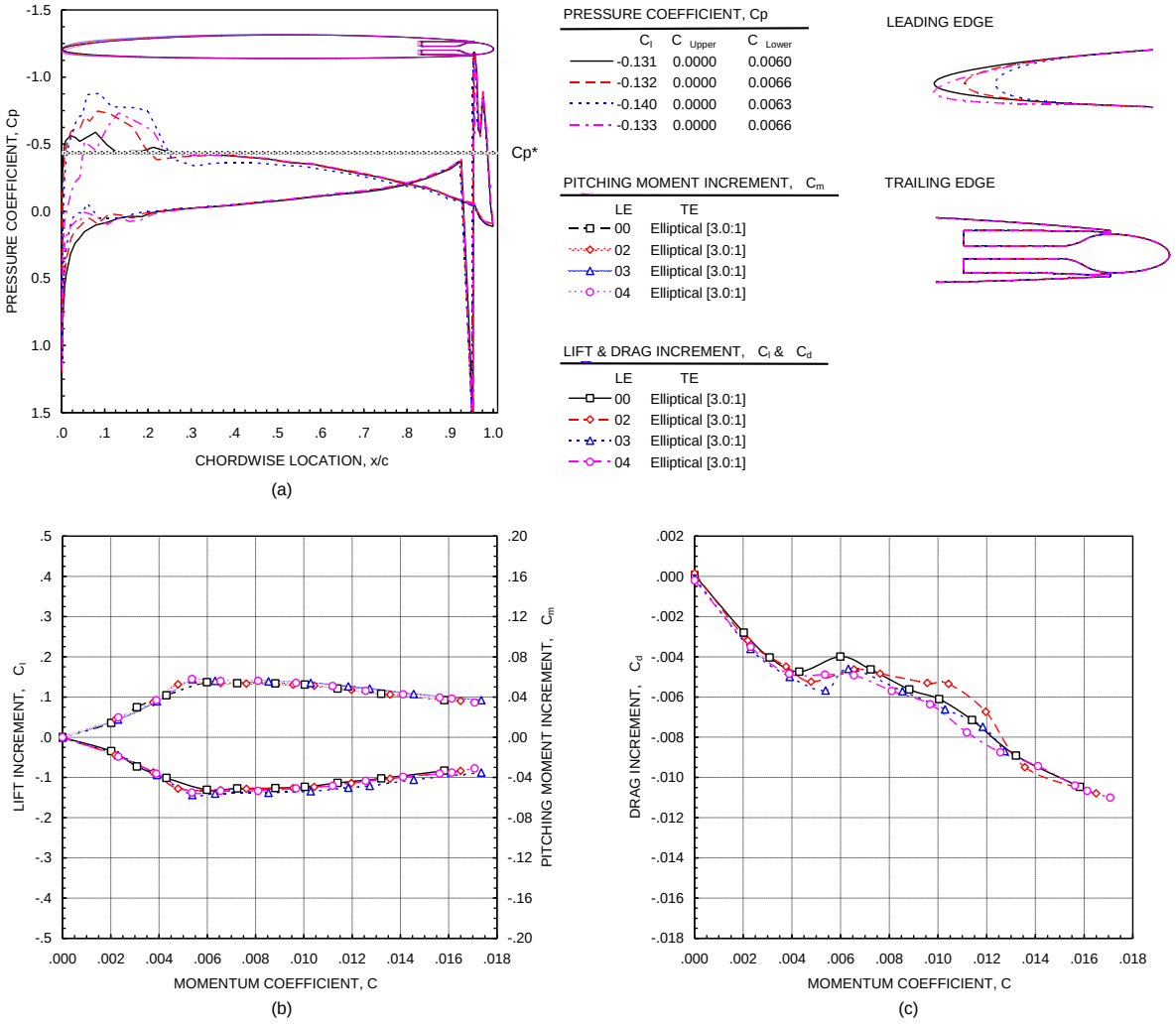

Figure 18. Airfoil performance at M = 0.8, = 3 , for lower-surface blowing for configurations having elliptical Coanda trailing-edge [3.0:1] and various leading-edge geometries.

References

[1]Novak, C. J.; Cornelius, K.C.; Road, R.K.: Experimental Investigations of Circular Wall Jet on a Circulation Control Airfoil. AIAA 87-0155, January 1987.

[2]Englar, R. J.; Circulation Control Pneumatic Aerodynamics: Blown Force and Moment Augmentation and Modification; Past, Present, & Future. AIAA 200-2541, June 2000.

[3]Englar, R. J.; Williams, R. M.: Test Techniques for High Lift, Two-Dimensional Airfoils with Boundary Layer and Circulation Control for Application to Rotary Aircraft. Naval Ship Research and Development Center, Report 4645, July 1975.

[4]Metral, A. R., "On the Phenomenon of Fluid Veins and their Application, the Coanda Effect," AF Translation, F-TS-786-RE, 1939.

[5]Sproule, R. S. and S.t. Robinson, "Combined Intelligence Objective Sub-committee report," WF Document Library Item 5, File No. IX-1, X-2, XII-1, D52.420/27, 1944.

[6]Voedisch, Alfred, Jr., 'Analytical Investigation of the Coanda Effect (Project No. FP-188)," Air Material Command, Wright Field, Dayton, Ohio, Report No. F-TR2155-ND, April 3, 1947.

[7]Englar, R. J.; Investigations Into and Application of the High Velocity Circulation Control Wall Jet for High Lift and Drag Generation on STOL Aircraft.. AIAA 74-502, June 1974.

[8]Cheesman, I.C.; and Seed, A.R.: The Application of Circulation Control by Blowing to Helicopter Rotors. *Journal of Royal Aeronautical Society*, Vol. 71, No. 848, July 1966.

[9]Englar, R.J.: Two Dimensional Transonic Wind Tunnel Tests of Three 15-Percent-Thick Circulation Control Airfoils. Naval Ship R&D Center Report ASED-182 (AD 882-075), December 1970.

[10]Mavis, D.N.; Kirby, M.R.: Takeoff/Landing Assessment of an HSCT with Pneumatic Lift Augmentation. AIAA-99-0534, Jan. 1999.

[11]Abramson, J.; Rogers, E.O.: High Speed Characteristics of Circulation Control Airfoils. AIAA 83-0265, Jan. 1983.

[12]Abramson, J.: The Low Speed Characteristics of a 15-Percent Quasi-Elliptical Circulation Control Airfoil with Distributed Camber. David W. Taylor Naval Ship R&D Center Report DTNSRDC/ASED-79/07 (ADA084-176), May 1979.

[13]Nielsen, J. N.; and Bigger, J. C.: Recent Progress in Circulation Control Aerodynamics. AIAA Paper 87-0001, Jan. 1987.

[14]Englar, R. J.: Circulation Control for High Lift and Drag Generation on STOL Airfoil. *Journal of Aircraft*, Vol. 12, No. 6, 1975, pp. 457-463.

[15]Englar, R. J.; Trobaugh, L. A.; and Hemmerly, R. A.: STOL Potential of the Circulation Control Wing for High Performance Airfoil. *Journal of Aircraft*, Vol. 15, No. 3, 1978.

[16]Nichols, J. H. Jr.; Englar, R. J.; Harris, M. J.; and Hason, G. G.: Experimental Development of an Advanced Circulation Control Wing System for Navy STOL Airfoil. ALKA Paper, 81-8151, 1981.

[17]Englar, Robert J.; Smith, Marilyn J.; Kelley, Sean M.; and Rover III, Richard C.: Application of Circulation Control Technology to Advanced Subsonic Transport Aircraft, Part I: Airfoil 14 Development. AIAA Paper No. 93-0644; *Journal of Aircraft*, Vol. 31, No. 5, Sept-Oct. 1994, pp. 1160-1168.

[18]Kind, R. J.; and Maull, D. J.: An Experimental Investigation of a Low-Speed Circulation-Controlled Aerofoil. *The Aeronautical Quarterly*, Vol. 19, May 1968, pp. 170-182.

[19]Wood, N. J.; and Nielsen, J. N.: Circulation Control Airfoil-Past, Present, and Future. AIAA Paper 85-0204, Jan. 1985.

[20]Englar, R. J., Hemmerly, R. A., Moore, H., Serendinsky, W., Valckenaere, J., & Jackson, J. A.; Design of the Circulation Control Wing STOL Demonstrator Aircraft, AIAA 79-1842, August 1979.

[21]Englar, R. J.; "Development of the A-6/Circulation Control Wing Flight Demonstrator Configuration," DTNSRDC Report ASED-79/01, January, 1979.

[22]Pugliese, A. J.; Flight testing the circulation control wing, AIAA. 79-1791, August, 1979.

[23]Alexander, M. G., Anders, S. G., Johnson, S. K., Florance, J. P., & Keller, D. F. Trailing Edge Blowing on a Two-Dimensional Six-Percent Thick Elliptical Circulation Control Airfoil Up to Transonic Conditions. NASA/TM-2005-213545. Hampton: Langley Research Center, (2005).

[24]Englar, R.J.; Williams, R.M.: Test Techniques for High Lift, Two-Dimensional Airfoils with Boundary Layer and Circulation Control for Application to Rotary Aircraft. Naval Ship Research and Development Center, Report 4645, July 1975.

[25]Baals, Donald D.; and Mourhess, Mary J.: Numerical Evaluation of the Wake-Survey Equations for Subsonic Flow Including the Effect of Energy Addition. NACA WR L-5 H27, 1945.

[26]Englar, R. J. and R.M. Williams.: Test Techniques for High-Lift Airfoils with Boundary Layer and Circulation Control for Application to Rotary Wing Aircraft. Canadian Aeronautics and Space Journal, Vol. 19, No. 3, pp. 93-108, March 1973.

[27]Rogers, E.O.: Development of Compressible Flow Similarity Concepts for Circulation Control Airfoils. AIAA-87-0153, January 1987.

[28]Hoerner, Sighard, F.: Fluid-Dynamic Lift. Hoerner Fluid Dynamics, 2nd Edition, June 1992.

[29]Blevins, Robert, D.: Applied Fluid Dynamics Handbook. Krieger Publishing Company, Reprint Edition June 2002.

[30]Holmes, J. D.: Transition Trip Technique Study in the McAir Advanced Design Wind Tunnel. Technical Memorandum 4395, May 1984.

[31]Staff, Aeroelasticity Branch.: *The Langley Transonic Dynamics Tunnel*. LWP-799, September 23, 1969.

[32]Krause, Lloyd, N.: *Effects of Pressure-Rake Design Parameters on Static-Pressure Measurements for Rakes Used In Subsonic Flow*. NACA-TN 2520, Oct. 1951.

[33]McLachlan, B.G.: *On The Effect of Leading-edge Blowing On Circulation Control Airfoil Aerodynamics.* Proceedings of the Circulation-Control Workshop, NASA Ames Research Center, NASA CP 2432, February 18-21, 1986.

[34]Raymer, Daniel P.: Aircraft Design: A Conceptual Approach. 3rd Edition, 1999.

[35]Staff of the Propulsion Aerodynamics Branch: *Data Reduction Formulas for the 16-Foot Transonic Tunnel*. Revision 2, NASA Technical Memorandum 107646, July 1992.